Journal of Marine Science and Technology

Volume 23 | Issue 5 Article 14

RAINFALL-INDUCED SLOPE LANDSLIDE PONTENTIAL AND LANDSLIDE DISTRIBUTION CHARACTERISTICS ASSESSMENT

Yung-Sheng Chue
Department of Civil Engineering, National Cheng Kung University, Tainan, Taiwan, R.O.C.

Jing-Wan Chen
Department of Civil Engineering, National Cheng Kung University, Tainan, Taiwan, R.O.C., geochen@mail.ncku.edu.tw

Yie-Ruey Chen
Department of Land Management and Development, Chang Jung Christian University, Tainan, Taiwan, R.O.C.

Recommended Citation

Chue, Yung-Sheng; Chen, Jing-Wan; and Chen, Yie-Ruey (2015) "RAINFALL-INDUCED SLOPE LANDSLIDE PONTENTIAL AND LANDSLIDE DISTRIBUTION CHARACTERISTICS ASSESSMENT," *Journal of Marine Science and Technology*: Vol. 23: Iss. 5, Article 14.
DOI: 10.6119/JMST-015-0529-3
Available at: https://jmstt.ntou.edu.tw/journal/vol23/iss5/14

RAINFALL-INDUCED SLOPE LANDSLIDE PONTENTIAL AND LANDSLIDE DISTRIBUTION CHARACTERISTICS ASSESSMENT

Acknowledgements

This work was supported in part by ROC Ministry of Science and Technology Grants NSC 101-2625-M-309-002 and MOST 102-2625-M-309-002. The writers wish to express their appreciation to Disaster Prevention Research Center, NCKU for providing technical support of ENVI.

Journal of Marine Science and Technology, Vol. 23, No. 5, pp. 705-716 (2015)
DOI: 10.6119/JMST-015-0529-3

RAINFALL-INDUCED SLOPE LANDSLIDE PONTENTIAL AND LANDSLIDE DISTRIBUTION CHARACTERISTICS ASSESSMENT

Yung-Sheng Chue[1], Jing-Wan Chen[1], and Yie-Ruey Chen[2]

Key words: landslide susceptibility, GANN, multivariate hazards evaluation method, GIS.

ABSTRACT

According to observations over the few years before and after typhoon and extreme rainfall events in the Laonong catchment of Kaohsiung, Southern Taiwan, this study combined a genetic adaptive neural network architecture, image texture analysis, and a geographic information system (GIS) in satellite image interpretation and land use change analysis to obtain disaster records and surface information. A multivariate hazards evaluation method was applied to quantitatively analyze the weights of various natural environmental and slope development hazard factors. Furthermore, this study established a slope landslide potential assessment model and depicted a slope landslide potential diagram by using the GIS platform. The impact of extreme rainfall events on slope landslide and landslide developmental characteristics were discussed. The findings can be a reference for subsequent slope development countermeasures and as an assessment for the academia and engineering fields involved in predicting landslide disasters caused by slope development.

I. INTRODUCTION

Because of poor physiographic conditions and steep mountainous terrain, concentrated rainfall accompanying typhoons and rainstorms can easily trigger landslides and debris flows in unstable regions. In recent years, because of extreme rainfall events, numerous slope landslides, heavy river siltation, and riverbank dikes have markedly changed the natural environmental conditions of catchment regions in Taiwan. In August 2009, Typhoon Morakot produced extremely heavy rainfall over Taiwan; the cumulative maximum rainfall in the southern Taiwan's mountainous region exceeded 2900 cm, causing severe landslides, debris flows, flooding, and slope collapses. This disaster critically affected inhabitants, damaged property and the living environment, and threatened major public construction projects, severely affecting overall industrial and economic development and transport pathways.

Slope landslide analyses generally explore primary hazard factors used for identifying the slope slide hazard factor combinations and establishing landslide potential assessment models. Several studies conducted in Taiwan and elsewhere have recently explored the hazard factors of slope landslides (Popescu, 2002; Wang and Sassa, 2006; Lee et al., 2008; Chen et al., 2009; Abay and Barbieri, 2012). Similar to other geological disasters, each landslide is caused by unique factors, comprising a few influencing factors such as potential causes (e.g., geological factors including soil, topography, and hydrology) and impetuses (e.g., rainfall, earthquakes, and anthropogenic factors). Geological factors include lithological factors, structural conditions, soil thickness, and cover situations; topographical factors include slope, aspect, and elevation location; and anthropogenic factors include timber harvesting, road construction, land development, mining, and vegetation changes. Studies have explored various factors used for assessing and estimating landslide factors from various perspectives. Although uncertainties continue to exist regarding various hazard factors, and certain challenges are difficult to overcome, these factors provide essential information for estimating the size of potential landslides.

Because technological advances afford numerous land use monitoring tools, in post disaster large-area slope disaster interpretation and judgment, aerial photography and satellite imagery are often used for risk interpretation and assessment (Nikolakopoulos et al., 2005; Lin et al., 2006; Chen et al., 2009; Chen et al., 2013). Because satellite imaging is characterized by short data acquisition cycles and rapid, wide, and low-cost capturing of ground surface changes using computer analyses and geographic information system (GIS) platforms, they can be utilized to quickly assess situations, particularly in mountainous and inaccessible areas. Therefore, satellite imaging is feasible for large-area survey applications and long-term land

Paper submitted 09/03/14; revised 04/13/15; accepted 05/29/15. *Author for correspondence: Jing-Wen Chen (e-mail: geochen@mail.ncku.edu.tw).*
[1] *Department of Civil Engineering, National Cheng Kung University, Tainan, Taiwan, R.O.C.*
[2] *Department of Land Management and Development, Chang Jung Christian University, Tainan, Taiwan, R.O.C.*

use change monitoring (Liu et al., 2001).

In recent years, scholars have published studies on using artificial neural networks (ANNs) in satellite image classification and landslide interpretation and assessment (Yoshida and Omatu, 1994; Jarvis and Stuart, 1996; Dymond et al., 1999; Chen et al., 2009; Chen et al., 2013); ANNs are advantageous and economical and extract more parametric information through learning and interaction capabilities. In addition, texture is a parameter of satellite images. In an image block, when local statistical properties or image characteristics remain unchanged, change slowly, or are approximately predicted, the texture is considered unchanged (Sklansky, 1978). Recently, scholars have used textural information as auxiliary information in satellite image interpretation to improve the degree of precision (Shen and Sarris, 2008; Chen et al., 2011).

In the past, scholars have applied the multivariate hazards evaluation method (HEM) (Su et al., 1998) in studies pertaining to the delineation of catchment landslide potential (Lin et al., 2009). HEM involves a multinonlinear mathematical model based on measurement as the primary concept. Using relative relationships, Lin et al. (2009) proposed a danger index (Dt) for assessing the risk of environmental hazards in different regions.

Genetic algorithms (GAs), a type of artificial intelligence (AI) proposed by Holland (1975), is an optimized search mechanism that functions on the basis of computer simulations of biological natural selection and genetic rules (Holland, 1975; Goldberg, 2007). GAs search for the desired parameters in the natural evolution process, including reproduction, crossover, and mutation. GAs differ from traditional numerical search methods in that GAs converts possible solutions into chromosomes by using an encoding technology and directly search the search space. Combined with specific search operators, GAs exchange information during the search, thus determining the global optimal solution.

Our study area covered various parts of the Laonong catchment in Kaohsiung, southern Taiwan. According to previous studies (Chen et al., 2010; Chen et al., 2013), this study applied a genetic ANN (GANN) in classifying satellite imagery, using the gray level co-occurrence matrix (GLCM) for extracting textural information from high-resolution satellite images to improve assessment and interpretation accuracy. Moreover, HEM was applied for quantitatively analyzing the weights of various hazard factors related to natural environmental and slope development to estimate the landslide susceptibility of the study area. Finally, GIS was used to describe the landslide susceptibility diagram and explore the impact of extreme rainfall events on slope landslide and development characteristics of the landslide region.

II. RESEARCH METHODS

1. Genetic Adaptive Neural Networks

An ANN is an AI technique combining the high computing speed, memory, and learning ability of advanced computing technologies. ANNs are ideal for processing highly complex nonlinear functions because of their simple training methods, lack of equation assumptions, and large-scale data processing abilities with high precision and speed. The back-propagation neural network model (BPN) used in this study is the most representative and widely used ANN learning model. The BPN is a three-layer neural network comprising input, hidden, and output layers and uses the gradient steepest descent method for minimizing the error function. Each layer accepts the output of the previous layer as its input, and the hidden layer contains a number of neurons. The layers are connected using weights and biases, and the BPN multiplies the input and the total weights. Obtained through the transfer function, the output value is compared with the target value, and the weighted value is modified using the algorithm to minimize the error function. The BPN activation function converts the output value range after superimposing the input values. The defined value maintains the neuron output values in a reasonable range through the conversion of the total sum of the implication of the input and weight. After referring to Chen et al. (2010) and Chen et al. (2013), this study used the tansig function as the activation function, and the set normalized output values ranged from −1 to 1.

In addition to the result being locally minimized rather than globally minimized, other drawbacks of using an ANN include inadequate training or overtraining and its inability to converge. To overcome these disadvantages, according to the studies by Chen et al. (2010) and Chen et al. (2013), parameters were optimized using GAs coupled with an ANN; the basic principle involved setting the ANN architecture parameters, including the weighting matrix, as the GA chromosomes (i.e., target solutions). This study adopted the difference between the network predicted and actual values as the fitness function of the algorithm by using the mean squared error as the criterion with which to assess chromosomal fitness. The actual values refer to the subcategories of the factors to be interpreted; the output classified the predicted spectral values of various sample regions through GANN simulations. Depending on the GA's ability to determine the optimal solution, a network structure that minimizes the error between the predicted and actual values was determined.

For GANN computation, this study adopted binary GA encoding as well as elitism selection and uniform crossover with 200 generations (the number of chromosome groups), which had been selected by other scholars (D'Ambrosio et al., 2006). The common selection rate is around 0.1 and the general crossover probability is primarily 0.5-0.8. Generally, a high mutation probability is similar to a random search. Heng et al. (1999) recommended a mutation rate between 0.1 and 0.001. To avoid the loss of the optimal search capability, the widely-used mutation rate of 0.1 was used in this study. A high mutation rate ensures a faster optimal solution search process, whereas a low mutation rate stalls the search process. According to Chen et al. (2009), this study adopted a crossover rate of 0.6. The BPN parameters are the number of hidden

layers and neurons, learning rate, and learning time. One hidden layer is adequate for general problems and two hidden layers can satisfy most problems. Therefore, the upper limit for the number of hidden layers was set as two. The operational speed is considerably reduced when the number of neurons exceeds 30 (Chen et al. 2009). Therefore, according to the operational bit limit, the upper limit of the number of neurons was set as 32. On the basis of testing experience, the network converges after 15,000 learning steps (Chen et al., 2013). Hence, the upper limit of the learning steps was set as 15,000 to enable the algorithm to search for the optimal solution in this range. Satisfying one of the following conditions ceased the search operation (Chen et al., 2013):

(1) The fitness function equals zero or the allowed value;
(2) All generations of percentages, excluding the mutation rates, satisfy the optimal fitness value without more than 1,000 evolutionary changes;
(3) The operational time reaches the set cumulative value.

2. Texture Analysis

In image analysis, the pixel grayscale values are of low order, and the mutual relationships between pixels, such as direction and rules, are of high order (i.e., texture); the image exhibits different textural features for various land cover types. This study applied the texture analysis function of ENVI (RSI, 2005) image processing software for establishing the GLCM and for satellite image quantification within the study area. The results were used for ANN image interpretation, training, and classification.

GLCM is a second-order statistical method used to sum the frequency of each grayscale value at specific relevant positions. The computational method is shown in Eq. (1) (Haralick et al., 1973):

$$C_{uj}(d,\theta) = \frac{P_{ij}(d,\theta)}{\sum_{i=0}^{N}\sum_{j=0}^{N} P_{ij}(d,\theta)} \tag{1}$$

where P_{ij} denotes the joint probability of grayscale values i and j at relative position (d, θ), d is the distance, and θ is the direction. Eq. (1) yields the textural eigenvalues.

Several methods exist for quantifying texture. Haralick et al. (1973) suggested various methods for quantifying the textural statistics of the GLCM matrix. The most widely applied textural quantification method, described in the following, was used in this study.

Homogeneity: used to measure textural uniformity. High uniformity yields high homogeneity.

$$Homogeneity = \sum_{i=0}^{N}\sum_{j=0}^{N} \frac{1}{1+(i \quad j)^2} C_{ij} \tag{2}$$

where subscripts i and j represent the grayscale values of the pixels, and C_{ij} is the value after GLCM computation.

Contrast: used to measure textural contrast. High textural contrast yields a low contrast value.

$$Contrast = \sum_{i=0}^{N}\sum_{j=0}^{N} (i \quad j)^2 C_{ij} \tag{3}$$

Dissimilarity: used to measure the image grayscale dissimilarity degree.

$$Dissimilarity = \sum_{i=0}^{N}\sum_{j=0}^{N} C_{ij} |i \quad j| \tag{4}$$

Entropy: used to measure the textural chaotic degree. A more random image texture yields a lower entropy.

$$Entropy = \sum_{i=0}^{N}\sum_{j=0}^{N} C_{ij} \log C_{ij} \tag{5}$$

Angular second moment (ASM): used to measure textural uniformity and evenness. A low ASM value indicates that the matrix elements are evenly distributed.

$$ASM = \sum_{i=0}^{N}\sum_{j=0}^{N} C_{ij} \tag{6}$$

This study employed the ENVI module for estimating textural information, such as homogeneity, contrast, dissimilarity, and the ASM of the red (R), green (G), blue (B), and near-infrared (NIR) spectra of satellite images of the study area. Spectral values extracted using ArcGIS were combined with standardized spectral values of the original images and input into the ANN for training and classification.

3. Multivariate Hazards Evaluation Method

Multivariate HEM is a measurement-based multivariate nonlinear mathematical model. Using relative relationships, HEM involves applying a danger index (D_t) as the risk indicator of environmental hazards in different regions of the study area.

To estimate the impact weights of the various hazard factors, the coefficient of variation (V) is obtained using the graded disaster-triggering ratio of the factors. The coefficient, which represents the sensitivity of the graded response to the landslide probability of various factors, is computed as shown in Eq. (7):

$$V = \frac{\sigma}{X} \times 100\% \tag{7}$$

where σ is the standard deviation and X is the average damage in the sample regions of various graded levels. The weight of a factor is calculated as the ratio of the coefficients of variation

of the factor to the total coefficient of variation of all factors, as shown in Eq. (8); the weights represent the degree of impact of each factor affecting the landslide.

$$W_i = \frac{V_i}{V_1 + V_2 + \cdots + V_n} \tag{8}$$

where W and V are the factor weight and coefficient of variation, respectively. The graded score values of hazard factors d, represented by relative values in the range of 1-10, is estimated using the damage percentages of the various factors, as shown in Eq. (9).

$$d_n = \frac{9\left(X_i - X_{\min}\right)}{\left(X_{\max} - X_{\min}\right)} + 1 \tag{9}$$

where X_i denotes the sample region's disaster-triggering rate, and $X_{\max}$ and $X_{\min}$ represent the maximal and minimal loss percentages of various sample regions, respectively.

Finally, the weights (W_i) are arranged according to the variation (V) to obtain different scores of the factors:

$$D_t = d_1^{W_1} \times d_2^{W_2} \times d_3^{W_3} \times d_4^{W_4} \times d_5^{W_5} \cdots\cdots \times d_n^{W_n} \tag{10}$$

where D_t is the danger index of the potential disaster represented by a relative value in the range of 1-10.

III. RAINFALL-INDUCED SLOPE LANDSLIDE ASSESSMENT MODELING

The rainfall-induced slope landslide assessment model for a catchment in southern Taiwan was constructed in seven stages, as elaborated in the following.

1. Selection of Study Area

In August 2009, Typhoon Morakot induced large-scale slope landslides in the eastern and southern regions of Taiwan, with the Kaohsiung-Pingtung region being the most affected. Moreover, in recent years, extreme rainfall has caused frequent slope landslides. Therefore, after such considerations as the numerous land disturbance factors associated with regions affected by typhoons and extreme rainfall and the satellite images before and after the rainfall, the rectangular area formed by the UTM coordinates (214115, 2559916) and (2239550, 2553630), covering Baolai Li (Liugui District) and Jianshan Li (Taoyuan District) in the watershed of the Laonongxi River (Fig. 1), was used as the study area. To explore whether the landslide region and the distribution of the landslide locations were unaltered after Typhoon Morakot, this study focused on the 3 years after Typhoon Morakot (2009 to 2011). During this period, the study area experienced six heavy rainfall events (24-h cumulative rainfall >130 mm): four typhoons and two heavy rainfall events.

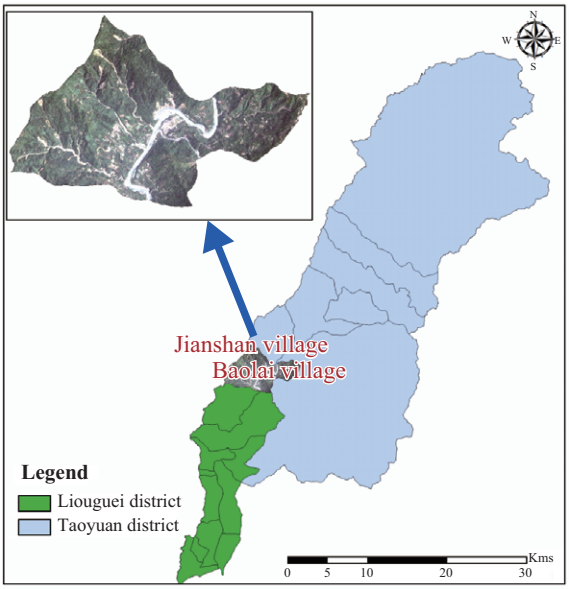

Fig. 1. Location and satellite image of the study area.

2. Constructing Original Image Data

The original image data of the Laonongxi River catchment (Baolai Li and Jianshan Li) region contains FM2 satellite images, digital elevation maps (DEMs), and geological maps before and after typhoons and heavy rainfall events. The relevant features and spatial data of the images were established through GIS integration.

According to the dates of heavy rainfall events recorded by the Central Weather Bureau of Taiwan, 12 satellite images were selected for the six events. Table 1 lists the basic data pertaining to these satellite images.

3. Establishing Basic Grid

The FM2 multispectral images used in this study have a spatial resolution of 2-8 m, whereas the DEM resolution is only 40 m × 40 m. Therefore, this study employed the GIS software ArcGIS to establish a 40 m × 40 m basic grid and the spatial analyst module to estimate the geological type and the average slope and elevation of each grid.

4. Selecting Influencing Factors

Regarding the environmental and anthropogenic factors affecting the slope landslide, a factor database was established according to the following natural environmental, triggering, and land disturbance factors for constructing the landslide potential assessment model:

(1) Natural Environmental Factors

Several slope landslide factors have been considered in previous studies. After a literature review, the most widely used, easily accessible, and most strongly influential slope landslide factors were selected as the major natural environmental factors affecting the landslide disaster potential: slope,

Table 1. Basic data associated with selected FM2 satellite images.

Event No.		Event Date	Image Shooting Date	Image Resolution
A		Before Typhoon Morakot (2009/08/05)	2009/5/9	2 m
		After Typhoon Morakot (2009/08/05)	2009/8/24	2 m
B	----	Before heavy rainfall (2010/7/27)	2010/5/25	2 m
	C	After heavy rainfall (2010/7/27) Before Typhoon Meranti (2010/9/9)	2010/8/10	2 m
----		After Typhoon Meranti (2010/9/9)	2010/9/11	2 m
D		Before Typhoon Fanapi (2010/09/17)	2010/9/11	8 m
		After Typhoon Fanapi (2010/09/17)	2010/11/21	8 m
E	----	Before Typhoon Meari (2011/6/23)	2011/5/8	2 m
	F	After Typhoon Meari (2011/6/23) Before Typhoon Nanmadol (2011/08/27)	2011/8/17	8 m
----		After Typhoon Nanmadol (2011/08/27)	2011/10/24	8 m

aspect, geology, elevation, distance from river, and slope roughness. The spatial analysis module of ArcGIS, recommended by Chen et al. (2013), was used to obtain and grade the average slope, aspect, and elevation in various unit grids. Moreover, the values were classified according to the strength of the geological factors on the basis of the geological descriptions and corresponding features. The classification encoding method summarizes the rock characteristics according to geological descriptions and relevant geological characteristics. Next, the geological rock characteristics and compression strength were used with the compression strength-weakness grade relationship proposed by the International Society for Rock Mechanics (1981) to categorize and encode the geological descriptions (Chen et al., 2013). ArcGIS was applied for computing the grid distance from the river, and the grids were sorted according to the distance. Wilson and Gallant (2000) proposed that the slope standard deviation within the round window can be used for measuring the slope change; it is of indicative significance in the measurement of slope undulations in a window of a specific radius. Windows with a large slope roughness indicate drastic changes in slopes, such as near river bluff cliffs, cliffs, and waterfalls. The slope roughness values are encoded according to grade.

(2) Rainfall Triggering Factors

Climatic factors generally include rainfall, temperature, and humidity. Concentrated or extended rainfall highly affects slope stability. Therefore, similar to the aforementioned natural environmental factors, rainfall is considered one of the conditional factors affecting slope landslide. In this study, record were collected from five rainfall measurement stations of the Central Weather Bureau (Biaohu, Jiaxian, Gaozhong, Xinfa, and Xinan) during the six typhoon and rainfall events (24-hour cumulative rainfall of 130 mm or more) during August 2009-October 2011 (Table 1). For rainfall data grading, the effective accumulative rainfall (EAR) near the five rainfall measurement stations was computed, the basic grid of the study area was superimposed using the ArcGIS spatial analyst module, and the average EAR of the various grids was estimated using the inverse distance weighted method. Finally, the inferred EARs of the grids were graded and encoded. As reported by Seo and Funasaki (1973), EAR was computed as the sum of the direct and previous indirect rainfall. Direct rainfall is the consecutive rainfall during the landslide, the cumulative rainfall from the first rain to the occurrence of the slope landslide disaster (i.e., the hour of the greatest rainfall in the major rainfall area). Previous indirect rainfall refers to the 7-day rainfall before the major rain; it is estimated as

$$\sum_{n=1}^{7} k^n P_n = P_b \tag{11}$$

where P_n is the rainfall over n days before the major rain (mm), and k is the diminishing coefficient, set as 0.9 in this study. The direct rainfall directly contributes to the occurrence of the slope landslide. Therefore, its contribution to the disaster is large and, thus, not discounted. EAR is estimated using the following equation:

$$EAR = P_r + P_b \tag{12}$$

where P_r is the direct rainfall.

(3) Land Disturbance Factors

Because land disturbance varies with place and time, disaster and surface information can be obtained through satellite image interpretation classification, as elaborated in the preceding sections. According to the two principles of importance and reasonable accessibility and the study by Chen et al. (2009), six factors—green coverage (grassland, forest) rate, agricultural land (paddies and upland) planting rate, fruit tree planting rate, bare ground density, building density, and road density—were used as the land disturbance factors contributing to slope landslides. According to Chen et al. (2009, 2012), the grid index for land disturbance is defined as

$$I_{DC} = \sum G_{DC} \times R \tag{13}$$

where G_{DC}, the grading of disturbance condition, is the score of the grid land disturbance factors and R is the percentage of the land disturbance factors accounting for the basic grid. The G_{DC} score is based on the score value proposed by Chen et al.

Table 2. Network training optimal architectural parameters.

Image Date	Number of the hidden layers	the 1st hidden layer number of neurons,	the 2nd hidden layer number of neurons,	learning rate	learning times	Training accuracy (%)
2009/05/09	2	22	29	3	14000	92.2
2009/08/24	2	22	29	2	15000	93.6
2010/05/25	2	26	27	1.4	10000	88.9
2010/08/10	2	30	15	3.1	10000	92.8
2010/09/11	2	31	28	2.1	9000	98.0
2010/09/11	2	7	6	1	9500	83.6
2010/11/21	2	8	8	0.9	3300	88.4
2011/05/08	2	28	17	1.8	15000	99.7
2011/08/17	2	8	7	0.5	9000	82.8
2011/10/24	2	8	7	0.5	9000	85.8

(2013). After estimation, I_{DC} values were automatically clustered using the clustering analysis tool and graded and encoded according to the clustering results.

5. Satellite Image Interpretation

(1) Preprocessing Satellite Images

(a) Image retrieval correction

Because the original FM2 satellite images are images of spectral wavelengths, the relevant parameters of the satellite images were input. After combination and coordinate correction by using ERDAS Imagine software (ERDAS, 2011), the images were converted to image files compatible with the GIS system.

(b) Removal of image clouds and shadows

To remove the effect of clouds on the image interpretation results, ArcGIS software and artificial drawing was applied to select the regions covered by clouds and shadows in the satellite images. Subsequently, the original satellite images and the selected clouds were incorporated in ERDAS Imagine for removal.

(c) Textural information processing

This study used software to compute the textural information of homogeneity, contrast, dissimilarity, entropy, and ASM for the study area. ArcGIS was used to extract textural and R, G, B, and NIR spectral information from satellite images for GANN image interpretation training and input value classification.

(d) Standardization

Before selection and drawing of the training sample regions, textural and R, G, B, and NIR spectral information and satellite images were standardized for image training and classification. The standardization equation is as follows:

$$S = \frac{x - mean}{std} \tag{14}$$

where S is the standardized value, x is the factor for standardization, *mean* is the average of the factor, and *std* is the factor's standard deviation.

Table 3. Image interpretation results.

Image Date	OA (%)	Kappa
2009/5/9	77.0	0.75
2009/8/24	78.7	0.77
2010/5/25	76.4	0.75
2010/8/10	75.2	0.73
2010/9/11	80.4	0.79
2010/9/11	79.6	0.78
2010/11/21	82.2	0.81
2011/5/8	74.6	0.72
2011/8/17	82.1	0.79
2011/10/24	81.3	0.80

(2) Sample Region Selection and Training

In the satellite images, sample regions of representative interpretation factors were selected and trained using GANN modules (Chen et al., 2013) developed on MATLAB (MATLAB, 2010). The study factors considered for obtaining disaster and surface information were river channels, water bodies, forests, grasslands, agricultural fields, fruit trees, buildings, and roads. Table 2 shows the optimal architectural parameters of the ten satellite images of the study area before and after the six events. As the results suggest, the average training accuracy, which represents the probability of correct classification at any point in the sample region, is as high as 91%.

(3) Image Interpretation Classification Results (Accuracy Evaluation)

According to the optimal network architecture of image interpretations obtained using the aforementioned GANN training, this study involved conducting interpretation classification of the ten satellite images of the study area. According to the methodology of Chen et al. (2009), the coefficient of agreement kappa (Cohen, 1960) and overall accuracy (OA) were used as the basis for calculating the interpretation classification accuracy. Table 3 lists the image interpretation OA

Table 4. Correlation test results of the slope landslide hazard factors.

	slope	aspect	elevation	EAR	I_{DC}	geology	distance from the river	slope roughness
slope	1	-.080**	.395**	-.013**	-.011**	.168**	-.190**	-.016**
aspect		1	.043**	-.008**	.000	.181**	-.103**	-.096**
elevation			1	-.008**	-.022**	.224**	-.360**	-.098**
EAR				1	.008**	-.002	.013**	-.003
I_{DC}					1	-.020**	.021**	-.002
geology						1	-.249**	-.023**
distance from the river							1	.029**
slope roughness								1

**. Correlation is significant at the 0.01 level (2-tailed).
*. Correlation is significant at the 0.05 level (2-tailed).

and kappa values of the ten satellite images. The image interpretation OA and the average kappa are approximately 80% and 0.77, respectively. According to a relevant study (Landis and Koch, 1977), the obtained image interpretation classification results are of medium and high accuracy and, thus, are acceptable.

6. Selecting Slope Landslide Location

This study used ArcGIS software and DEM for projecting the ridgeline of the study area. If the area of bare land in the images before and after a typhoon or heavy rain event accounts for more than half of the grid area, and the normalized difference vegetation index (NDVI) of the images is less than 0, then the grid is considered the landslide location. The NDVI is used to evaluate the vegetation coverage, generally highlighting the differences in vegetation-covered areas by enhancing the strong NIR spectral reflection of plants, which absorb red light; it is therefore used for plant resources (Rouse et al., 1973; Mantovani et al., 1996). The NDVI is estimated as the ratio of *R* and NIR light. The projection relationship equation is

$$\mathrm{NDVI} = \frac{\mathrm{NIR} - R}{\mathrm{NIR} + R} \tag{15}$$

According to the method of Meunier et al. (2008), the distances between the landslide region peak and the nearest ridgeline top (*dr*), between the lowest point of the landslide region and the nearest river (*ds*), and between the ridge top and the river (*dt*) were obtained to evaluate the causes of and information relevant to landslides in the study area.

7. Constructing Slope Landslide Assessment Model

HEM was applied in the quantified evaluation of slope landslide potential, and the construction process is described as follows:

(1) Test of Factors

As mentioned previously, slope, aspect, geology, elevation, distance from river, slope roughness, EAR, and the index of land disturbance factors were used as factors in the slope landslide potential model. The Pearson correlation testing tool of SPSS statistical software (SPSS, 2005) was employed for determining the correlations among the hazard factors; Table 4 details the results for a rainfall event (2009 Typhoon Morakot). Regardless of the rainfall event, the factors were either correlated to a low degree (correlation coefficient = 0.1-0.4) or were not correlated (correlation coefficient ≤ 0.1).

(2) Assessment Model Construction Results and Analysis

(a) Computing factor weight score

As described previously, multivariate HEM was used to establish the slope landslide potential model. Table 5 lists the weight scores of the landslide potential factors. In the following, the factor weight score projection is explained using the slope factor as an example. The study area has slopes of seven grades. The table presents the grids in each grade and the number of landslides and damage percentages. After projecting the damage percentage standard deviation (σ = 0.011), Eqs. (7) and (8) were used to project the coefficient of variation (V = 0.714) and factor weight (W = 0.122), respectively. Finally, according to the maximal and minimal damage percentages of the slope factors, the grades of the slope factors were projected using Eq. (9). The weights and scores of various factors were computed similarly. The weight of geology (0.265) was the highest, whereas that of slope roughness (0.018) was the lowest. Moreover, the landslide ratio was the highest when the slope grade was 4 (slope > 30%-40%).

(b) Danger index modeling

After analysis, the weights of the eight slope landslide potential factors were ranked, in descending order, as follows: geology (G_s), aspect (A_s), EAR (EAR), slope (S), degree of land disturbance (I_{DC}), distance from river (D_r), elevation (E_l), and slope roughness (R_s). The established multivariate HEM assessment model is expressed in Eq. (16):

Table 5. Weights of landslide susceptibility factors.

Influencing factors	Factor grade	Total number of grids	total number of landslides	landslide ratio	score	Influencing factors	Factor grade	Total number of grids	total number of landslides	landslide ratio	score
slope (S_s)	1	6654	135	0.020	7.625	elevation (E_l)	1	270	8	0.030	9.770
	2	18180	318	0.017	6.711		2	29814	449	0.015	1.000
	3	55818	1096	0.020	7.411		3	27948	576	0.021	4.341
	4	29568	815	0.028	10.000		4	20772	570	0.027	8.452
	5	5130	124	0.024	8.892		5	16752	295	0.018	2.535
	6	0	0	0.000	1.000		6	11862	356	0.030	10.000
	7	0	0	0.000	1.000		7	7932	234	0.030	9.692
	standard deviation = 0.011			coefficient of variation = 0.714			standard deviation = 0.006			coefficient of variation = 0.261	
	Weight = 0.122						Weight = 0.045				
distance from the river (D_s)	1	2778	41	0.015	1.000	aspect (A_s)	1	12	2	0.167	10.000
	2	5382	85	0.016	1.436		2	8796	230	0.026	1.513
	3	10750	218	0.020	3.328		3	25578	628	0.025	1.417
	4	16684	277	0.017	1.778		4	26514	468	0.018	1.000
	5	23414	449	0.019	2.863		5	34452	643	0.019	1.061
	6	32158	545	0.017	1.923		6	19998	517	0.026	1.495
	7	24184	873	0.036	10.000		standard deviation = 0.058			coefficient of variation = 1.265	
	standard deviation = 0.007			coefficient of variation = 0.369			Weight = 0.216				
	Weight = 0.063										
Geology (G_s)	1	0	0	0	1.000	EAR	1	0	0	0.000	1.000
	2	0	0	0	1.000		2	21837	795	0.036	8.677
	3	69368	1525	0.022	10.000		3	20036	133	0.007	2.400
	4	45982	963	0.021	9.574		4	52300	739	0.014	3.980
	5	0	0	0	1.000		5	2245	13	0.006	2.221
	6	0	0	0	1.000		6	18932	808	0.043	10.000
	standard deviation = 0.011			coefficient of variation = 1.55			standard deviation = 0.017			coefficient of variation = 1.004	
	Weight = 0.265						Weight=0.172				
Slope roughness (R_s)	1	12840	242	0.019	1.000	I_{DC}	1	8588	205	0.024	2.320
	2	38280	761	0.020	3.175		2	98818	1860	0.019	1.000
	3	64230	1485	0.023	10.000		3	7944	423	0.053	10.000
	standard deviation = 0.002			coefficient of variation = 0.108			standard deviation = 0.019			coefficient of variation = 0.0581	
	Weight = 0.018						Weight = 0.099				

$$D_t = d\left(G_s\right)^{0.265} \times d\left(A_s\right)^{0.216} \times d\left(EAR\right)^{0.172} \times d\left(S_s\right)^{0.122} \times d\left(I_{DC}\right)^{0.099} \times d\left(D_s\right)^{0.063} \times d\left(El\right)^{0.045} \times d\left(R_s\right)^{0.018} \quad (16)$$

where $d(G_s)$ is the score of the geology-influencing grid factors; similarly, the remaining variables denote the scores of the other influencing grid factors. The equation clarifies that the influence of geology is the strongest, as reported by most scholars, followed by that of EAR and aspect. Rainfall is a critical slope landslide triggering factor, and aspect is associated with seasonal variations. The influence of the front aspect on the slope landslide is more pronounced than that of the back aspect. The influence of the slope and degree of land disturbance on the slope landslide are similar because historical rainfall-induced landslides were closely associated with the degree of land disturbance. Furthermore, because of climate changes, the type and speed of vegetation distribution and weather erosion varied with elevation. Development around rivers is often accompanied by soil and bank

erosion. All of these factors directly or indirectly affect slope stability.

IV. DRAWING AND VERIFICATION OF LANDSLIDE DISASTER POTENTIAL DIAGRAMS

The danger index assessment model (Eq. (16)) was used to investigate the slope landslide potential factor of each grid and estimate D_t; the average D_t values of the same grid locations for the six rainfall events ranged from 3.415 to 5.782. Log normal distribution was applied to convert the obtained potential grades to the landslide probability values by using multivariate HEM. The log normal distribution for computing potential grade probability is expressed as

$$P(F) = \frac{1}{\sqrt{2\pi}} e^{-\frac{1}{2}[(\ell nx - \mu/\sigma]^2} \tag{17}$$

where x is the grade of the danger index, and μ and σ are the average and standard deviation of the danger index grades, respectively. The potential grade probability estimated using log normal distribution ranged from 0.498 to 0.762. After standardization with Eq. (18), the probability ranged from 0 to 1.

$$P(F)' = \frac{(X_i - X_{\min})}{(X_{\max} - X_{\min})} \tag{18}$$

where X_i is the factor for standardization and $X_{\max}$ and $X_{\min}$ are maximal and minimal values of the landslide potential factors, respectively. After estimating the potential grades to the landslide probability values in each grid of research area by using Eq. (17), and standardizing by using Eq. (18), we applied clustering analysis (SPSS, 2005) to automatically categorize the landslide disaster potential grades into four categories: low, medium-low, medium-high, and high landslide potential. In addition, to verify the constructed slope landslide assessment model, several instances and types of major slope landslides that occurred in the study area in recent years were selected from the major landslide and debris flow information provided by the landslide disaster prevention information network of the Water and Soil Conservation Bureau of the Agricultural Council, Executive Yuan. GIS images of the landslide locations and the projected landslide potentials were used to conduct a superimposed imagery comparison. Fig. 2 shows the landslide-affected regions and the potential landslide regions in the superimposed images. Nearly 70% of the affected regions are located in the medium-high and high landslide potential regions.

V. ANALYSIS OF THE LANDSLIDE REGION DEVELOPMENTAL CHARACTERISTICS

Combining the collected data regarding the slope landslides

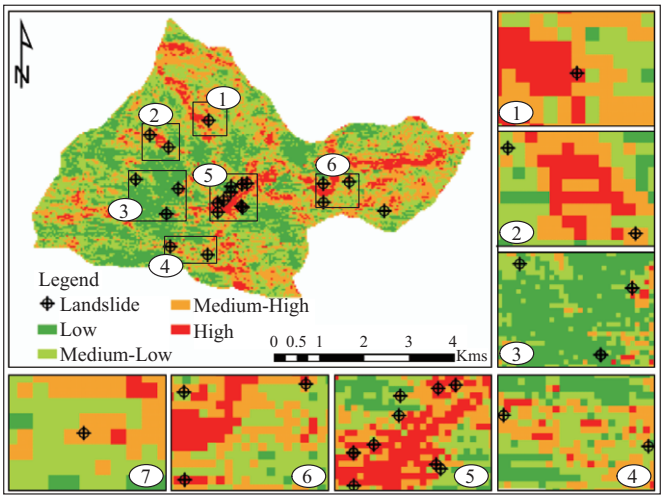

Fig. 2. Superimposed landslide potential regions and locations of landslide disasters.

triggered by the six typhoon and rainfall events, the landslide location interpretation results, and the application of the digital topographical diagrams of the study area, this study explored the landslide location developmental characteristics. Following Meunier et al. (2008) and according to the satellite image interpretation and landslide location judgment results before and after the typhoon and rainfall events, the distances between the landslide region peak (or bare land) and the nearest ridge top (dr), between the lowest point in the landslide and the nearest river (ds), and between the ridge top to the river (dt) were obtained. Fig. 3 presents the changes in (dr/dt), (ds/dt), and landslides.

The diagrams illustrate the distribution of landslides triggered by the six typhoon and rainfall events during 2009-2011. A comparison of the number and area of landslides at various periods revealed that the number and area of landslides increased substantially after rainfall. In particular, the distribution of landslides before and after the rainfall of the 2009 Typhoon Morakot (Table 1, Event A; Figs. 3(a) and 3(b)) was the highest. Fig. 3(b) shows that the number and area of landslides in the study area increased drastically after Typhoon Morakot, with large-area landslides occurring. Moreover, differences in the bare land spatial distribution before and after the six events facilitated analyses of the bare land restoration before each rainfall event. Fig. 3 shows that the slope bare land in the study area reduced after the rainy season of the year (Figs. 3(b) and 3(g)) as vegetation recovery was apparent.

Changes in the landslide locations are clear in the figures. Landslide locations biased toward the Y axis ($dr/dt = 0$) denote that the landslide started in the direction of the ridgeline. Conversely, landslide locations biased toward the X axis ($ds/dt = 0$) denote that the landslide extended along the river. The pre-Event A distribution depicted in Fig. 3(b) clarifies that most of the bare land in the study area is located near the river. However, after the landslide, the distribution is relatively even, with large bare land areas located near the river. As shown in

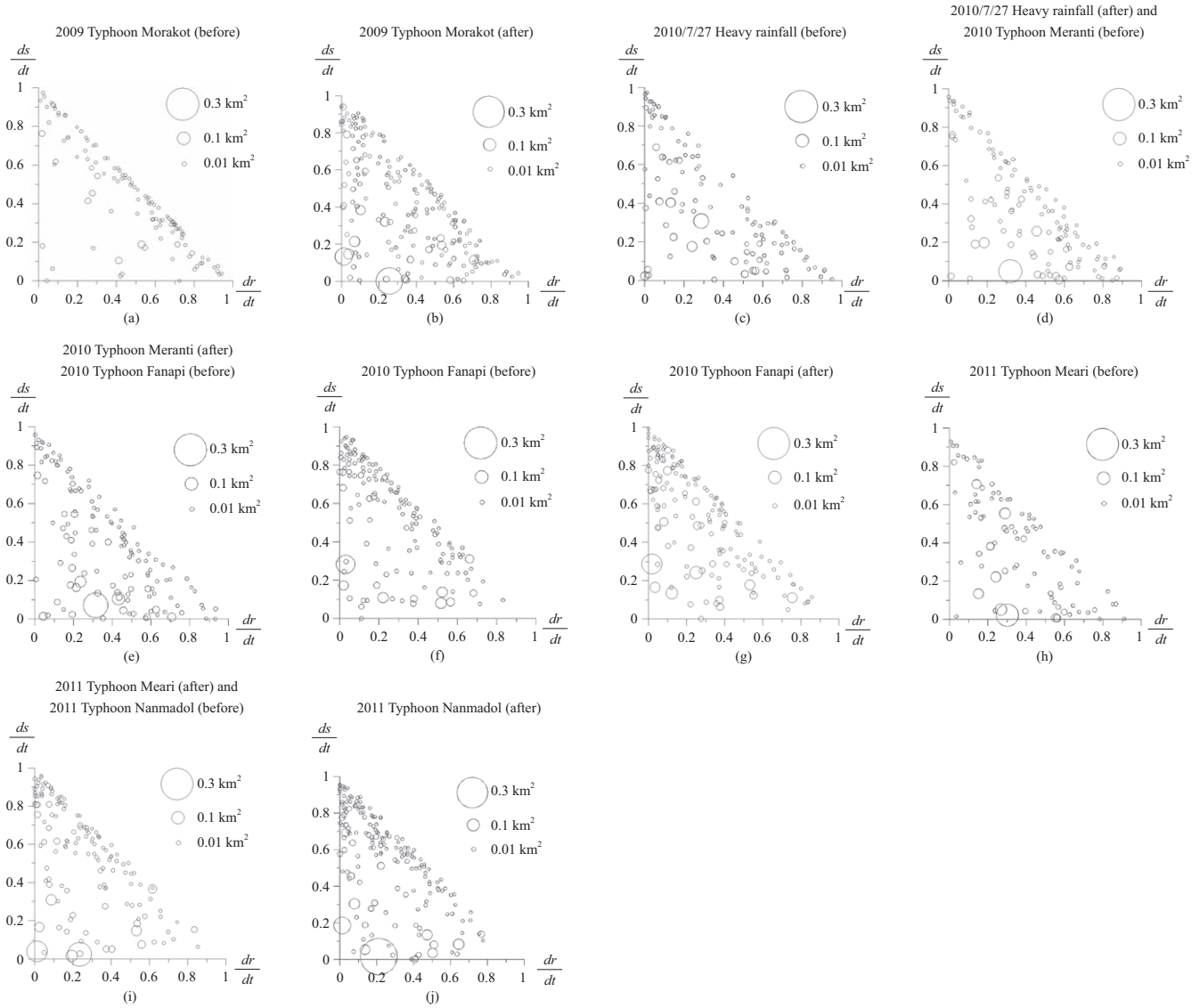

Fig. 3. Changes in *dr/dt*, *ds/dt*, and landslide range of the study area before and after the six rainfall events over 3 years.

Figs. 3(c) and 3(d), certain small bare land plots are present near the ridge top. After Event B, landslides occurred near the river with large-sized bare land plots. According to Fig. 3(e), after Event C, although the area of the bare land increased, the locations changed slightly. As shown in Figs. 3(f) and 3(g), before and after Event D, most bare land was located near the ridge top, similar to the case in Events E (Figs. 3(g) and 3(h)) and F (Figs. 3(i) and 3(j)). However, after rainfall Events E and F, medium and large bare land areas developed near the river.

VI. CONCLUSION

This study applied GANN to interpret and classify satellite images associated with six typhoon and rainfall events over three consecutive years. Moreover, multivariate HEM was adopted to establish a slope landslide potential model, and the landslide spatial distribution characteristics of the study areas were explored. The findings of the study are summarized as follows:

(1) GANN, multivariate HEM, and GIS were successfully applied in integrating and constructing a slope landslide potential evaluation process.
(2) This study applied GANN to interpret and classify satellite images of six typhoon and rainfall events for obtaining the disaster and land surface use information. The image interpretation classification OA was nearly 80% and the average consistency index kappa value was 0.77, suggesting acceptable accuracy at medium elevations.
(3) This study applied the multivariate HEM in the successful evaluation of slope landslide potentials. The landslide potential factors were slope, aspect, elevation, geology, EAR, index for land disturbance, distance from river, and

slope roughness. A correlation test confirmed the low correlation among these factors. The established assessment model revealed that the influence of geological factors is the strongest, followed by that of aspect and EAR. The influence of slope and the degree of land disturbance on slope landslides are similar.

(4) The projected danger index grade and standardized slope landslide probability are positively correlated. Moreover, this study applied GIS in describing the landslide potential probability diagram of the study area, revealing that nearly 70% of the regions damaged by the rainfall-induced landslides are located in the regions of medium-high or high landslide potentials.

(5) This study successfully adopted the GIS tool module of ArcGIS and DEM to evaluate the ridge lines. Furthermore, through satellite image interpretation, the landslide location spatial distribution data before and after rainfall at six different periods were obtained. The findings suggest that the number and area of landslides substantially increased compared with those before the rainfall events. In addition, bare land restoration analysis revealed that the slope bare land exhibited vegetation restoration after the rainy season.

(6) The analysis results of the rainfall-induced landslide spatial distribution characteristics suggest that medium and large landslide areas appeared to extend to the river after the rainfall events, although some landslides developed in the direction of the ridge top.

ACKNOWLEDGMENTS

This work was supported in part by ROC Ministry of Science and Technology Grants NSC 101-2625-M-309-002 and MOST 102-2625-M-309-002. The writers wish to express their appreciation to Disaster Prevention Research Center, NCKU for providing technical support of ENVI.

REFERENCES

Abay, A. and G. Barbieri (2012). Landslide susceptibility and causative factors evaluation of the landslide area of Debresina, in the Southwestern Afar Escarpment, Ethiopia. Journal of Earth Science and Engineering 2, 133-144.

Chen, J. W., Y. S. Chue and Y. R. Chen (2013). The application of genetic adaptive neural network in landslide disaster assessment. Journal of Marine Science and Technology 21(4), 442-452.

Chen, Y. R., J. W. Chen, S. C. Shih and P. N. Ni (2009). The application of remote sensing technology to the interpretation of land use for rainfall-induced landslides based on genetic algorithms and artificial neural networks. IEEE Journal of Selected Topics in Applied Earth Observations and Remote Sensing 2(2), 87-95.

Chen, Y. R., S. C. Hsieh and C. H. Liu (2010). Simulation of stress-strain behavior of saturated sand in undrained triaxial tests based on genetic adaptive neural networks. Electronic Journal of Geotechnical Engineering 15(Q), 1815-1834.

Chen, Y. R., S. C. Hsieh, K. J. Tsai and W. C. Lin (2012). Construction of evaluation model for landslide potential after rainfall due to slope land use. Proceeding of the 11th International & 2nd North American Symposium on Landslide, Banff, Alberta, Canada, 479-486.

Chen, Y. R., W. C. Lin and S. C. Hsieh (2011). Construction of an evaluation model for landslide potential due to slope land use: Case study of Baolai following Typhoon Morakot. Journal of Chinese Soil and Water Conservation 42(3), 251-262. (in Chinese, with English Abstract)

Chen, Y. R., P. N. Ni and K. J. Tsai (2013). Construction of a sediment disaster risk assessment model. Environmental Earth Sciences 70(1), 115-129.

Cohen, J. (1960). A coefficient of agreement for nominal scales. Educational psychology Measurements 20, 37-46.

D'Ambrosio, D., W. Spataro and G. Iovine (2006). Parallel genetic algorithms for optimizing cellular automata models of natural complex phenomena: An application to debris flows. Computer and Geosciences 32, 861-875.

Dymond, J. R., M. R. Jessen and L. R. Lovell (1999). Computer simulation of shallow landsliding in New Zealand hill county. International Journal of Applied Earth 1(2), 122-131.

ERDAS (2011). ERDAS IMAGE Tour Guide. ERDAS World Headquarter, Atlanta.

Goldberg, D. E. (2007). Genetic Algorithms in Search, Optimization, and Machine Learning, Addison-Wesley, Reading.

Haralick, R. M., K. Shaunmmugam and I. Dinstein (1973). Textural features for image classification. IEEE Transactions on Systems, Man, and Cybernetics 3(3), 610-620.

Heng, L., J. N. Cao and P. E. Love (1999). Using machine learning and GA to solve time-cost trade-off problem. Journal of Construction Engineering and Management 125, 347-353.

Holland, J. H. (1975). Adaptation in Natural and Artificial Systems. The University of Michigan Press.

ISRM (1981). Rock Characterization Testing and Monitoring: ISRM Suggested Method. Pergamon Press, London.

Jarvis, C. H. and N. Stuart (1996). The sensitivity of a neural network for classifying remotely sensed imagery. Computers and Geosciences 22(9), 959-967.

Landis J. R. and G. G. Koch (1977). The measurement of observer agreement for categorical data. Biometrics 33(1), 159-174.

Lee, C. T., C. C. Huang, J. F. Lee, K. L. Pan, M. L. Lin and J. J. Dong (2008). Statistical approaches to storm event-induced landslide susceptibility. Natural Hazard and Earth system Sciences 8, 941-960.

Lin, C. W., S. H. Liu, S. Y. Lee and C. C. Liu (2006). Impacts of Chi-Chi earthquake on subsequent rainfall-induced landslides in central Taiwan. Engineering Geology 86, 87-101.

Lin, F. L., J. R. Lin and Z. Y. Lin (2009). A Zonation Technique for Landslide Susceptibility in Watershed. Journal of Chinese Soil and Water Conservation 40(4), 438-453. (in Chinese)

Liu, H. Y., J. X. Gao and Z. G. Li (2001). The advances in the application of remote sensing technology to the study of land covering and land utilization. Remote Sensing for Land and Resources 4, 7-12.

MATLAB (2010). User Guide. The Mathworks, Inc..

Mantovani, F., R. Soeters and C. J. V. Westen (1996). remote sensing techniques for landslide studies and hazard zonation in Europe. Geomorphology 15, 213-225.

Meunier, P., N. Hovius and J. A. Haines (2008). Topographic site effects and the location of earthquake induced landslides. Earth and Planetary Science Letters 275, 221-232.

Nikolakopoulos, K. G., D. A. Vaiopoulos, G. A. Skianis, P. Sarantinos and A. Tsitsikas (2005). Combined use of remote sensing, GIS and GPS data for landslide mapping. Proceeding of IEEE International Geoscience and Remote Sensing Symposium, IGARSS '05, 5196-5199.

Popescu, M. E. (2002). Landslide causal factors and landslide remedial options. Keynote Lecture. Proceeding of the 3rd International Conference on Landslides, Slope Stability and Safety of Infra-Structures, Singapore, 61-81.

Rouse, J. W., R. H. Haas, J. A. Schell and D. W. Deering (1973). Monitoring vegetation system in the great plans with ERTS. Proceeding of the 3rd ERTS Symposium, NASA SP-351 1, 309-317.

RSI (2005). ENVI Practical Handbook.

Seo, K. and M. Funasaki (1973). Relationship between sediment disaster

(mainly debris flow damage) and rainfall. International Journal of Erosion Control Engineering 26(2), 22-28.
Shen, G. and A. Sarris (2008). Application of texture analysis in land cover classification of high resolution image. IEEE Fifth International Conference on Fuzzy Systems and Knowledge Discovery, 513-517.
Sklansky, J. (1978). Image segmentation and feature extraction. IEEE Transactions on Systems, Man, and Cybernetics. 8(4), 238-247.
SPSS (2005). Brief Guide. SPSS Inc.
Su, M. B., H. S. Tsai and L. B. Jien (1998). Quantitative assessment of hillslope stability in a watershed. Journal of Chinese Soil and Water Conservation 29(2), 105-114. (in Chinese, with English Abstract)
Wang, H. B. and K. Sassa (2006). Rainfall-induced landslide hazard assessment using artificial neural networks. Earth Surface Processes and Landforms 31(2), 235-247.
Wilson, J. P. and J. C. Gallant (2000). Terrain Analysis. John Wiely & Sons, New York.
Yoshida, T. and S. Omatu (1994). Neural networks approach to land cover mapping. IEEE Transactions on Geoscience and Remote Sensing 32(5), 1103-1109.